Complex Dynamics of Magnetic Billiards in a Torus

Albert Šilvans, s3400166

September 15, 2023

Contents

List of Figures

1 Introduction

Mathematical billiards is a broad topic in dynamical systems which studies the long term motion of a particle in the presence of an obstruction. The obstruction can be a boundary upon which the particle collides and then is elastically reflected, or there can be a vector field that deflects the particle, for example, a magnetic field. In this paper we consider the latter. We take the work [KS17] and [Gas21] as inspiration.

Let $H : \mathbb{R}^3 \times \mathbb{R}^3 \to \mathbb{R}$ be a magnetic Hamiltonian function:

$$H(q,p) = \frac{1}{2}\left\|p - A(q)\right\|^2 \tag{1}$$

where $q = (q_1, q_2, q_3)$ is position, $p = (p_1, p_2, p_3)$ is momentum, $A : \mathbb{R}^3 \to \mathbb{R}^3$ is a magnetic vector field defined as follows:

$$A(q) = (-b(q_2 \mod 1), 0, 0)\mathbb{1}_S(q \mod 1) \tag{2}$$

$$S = \{x \in \mathbb{R}^2 : \|x - 1/2\| \leq R\}, \tag{3}$$

with magnetic field strength $b \in (0, \infty)$, and $R \in (0, 1/2)$, the radius of the disk S centered at $(1/2, 1/2)$ in the plane. Lastly, $\mathbb{1}_S$ is an indicator function on S, that is $\mathbb{1}_S(x) = 1$ if $x \in S$ and $\mathbb{1}_S(x) = 0$ otherwise.

We note that A is independent of q_3, so for $q_3 = p_3 = 0$, a solution of the Hamiltonian equations of H is contained within the q_1q_2-plane. So, we ignore the q_3 variable completely. Furthermore, A is 1-periodic in both q_1 and q_2, so we can consider H on the torus $\mathbb{T} = \mathbb{R}^2/\mathbb{Z}^2$ via the quotient. We will refer to H on either surfaces interchangeably. Likewise, the periodicity of A gives rise to a lattice of disks centered at the points $N + 1/2$ for $N \in \mathbb{Z}^2$, we use the variable S to refer to either the disc in $[0, 1]^2$ or to the lattice, and make it clear which we are referring to when necessary.

The motion of a particle under H in the interior and the exterior of S is well understood. In the exterior of S there is no magnetic field, so the particle experiences free motion and travels in a straight line. In the interior of S, we know that the particle travels along arcs of a *Larmor* circle with *Larmor* radius $\|p\|/b$. Since eq. (1) is discontinuous along the boundary ∂S, we have an issue when considering particles that enter ∂S tangentially, in which case the solution is not necessarily unique. In such cases, we assume the particle is in free motion.

We see an example trajectory in fig. 1 which demonstrates the types of motion exhibited by the system. In blue we indicate free motion, and in red we have motion in the magnetic field. The red segments should instead be circular arcs, we reserve some artistic liberty in this choice. We also only draw the boundary of disks that are hit by the particle, and skip the rest to improve legibility. Focusing now on the trajectory itself we see:

- erratic behavior, that is, the trajectory seems to bounce around in a chaotic manner;
- evidence for quasi-periodic motion, specifically referring to the spot where the particle is trapped between four discs before eventually escaping;
- two distinct scales, the intervals of magnetic motion serve as a perturbation or deflection and are rather local, while the intervals of free motion

can be long and in fact can be arbitrarily long provided that the particle exits a disc at a shallow enough angle.

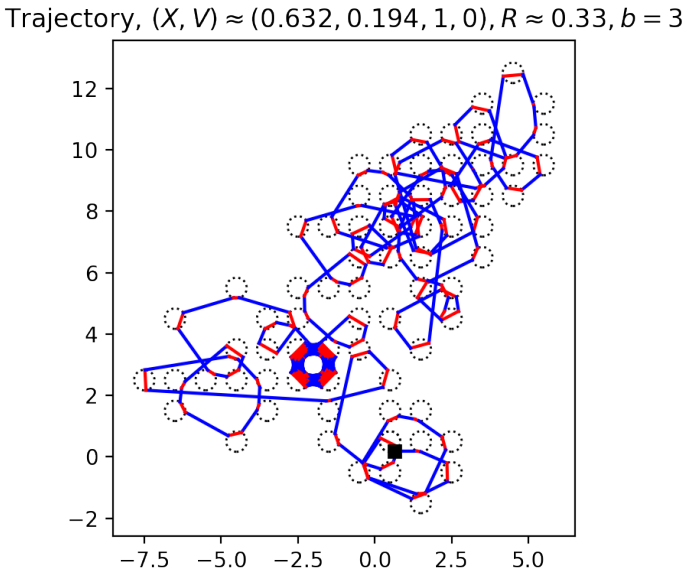

Figure 1: An example trajectory illustrating various types of motion.

So far, we see that the motion is not trivial, and warrants study. What is not yet evident from fig. 1 is the influence of the parameters R and b on the general behavior of the system. This is what we aim to better understand by the end of the paper.

We outline how we study this system. We focus on varying b, and identify three modes. For some $b_1, b_2 \in \mathbb{R}$ with $0 < b_1 \ll 1 < b_2$ we can also just suggest some values, given our observations,

1. If $0 < b < b_1$, the field strength is low. We can use KAM theory to make sense of quasi-periodicity at these strengths. We find two approaches using KAM.

2. If $b_1 < b < b_2$, the field has moderate strength and there is quasi-periodicity of varying complexity. We study this mode, and the next using symbolic dynamics and the Lempel-Ziv complexity measure.

3. If $b_2 < b$, the field is strong, and though periodic solutions can be found, we cannot find stable ones.

2 Weak magnetic fields and KAM theory

We begin by recalling Kolmogorov-Arnold-Moser (KAM) theory, state one of the main KAM theorems, and briefly outline the main points of the theory before delving into its application. We refer the reader to [Kna18] and [Ser22] for a more detailed account. We strongly recommend [Pö82] for reference, as it is the version of KAM we use here. What we will see is that for "small" values of b, our system (1) can be viewed as a perturbation of at least two different Hamiltonian systems, which can explain certain behavior we find. We corroborate our reasoning with many numerical simulations.

2.1 Summary of KAM theory

KAM theory is a method for studying perturbations of integrable Hamiltonian systems. Its origins lie in Celestial and Hamiltonian mechanics, where it was used to study the orbits of planets. Hamiltonian mechanics is a strong tool for modeling and studying systems, however it is strongest for conservative systems. Naturally, we find in practice many non-conservative systems, or conservative ones that are too complicated in full, in which case a smaller subsystem is modeled and the rest is viewed as a perturbation. We are interested in the second scenario, we denote by $H^0(q,p)$ an integrable Hamiltonian and by $H^1(q,p,\varepsilon)$ a perturbation.

Focusing on the integrable case, it is known by the Liouville-Arnold theorem that there exist *action-angle* coordinates so that $H^0 := H^0(p)$ can be expressed in terms of the action variable only. The equations of motion in action-angle coordinates are given by:

$$\dot{q} = \omega, \qquad \dot{p} = 0,$$

where $\omega = \partial_p H^0(p)$ and $\partial_p H^0 : I \to \Omega$ is the so-called *frequency map*. In these action-angle coordinates, the phase space becomes $\mathbb{T}^n \times I$ where $I \subseteq \mathbb{R}^n$ and the dynamics of the system are completely expressed as rotations on the torus. Specifically, phase space is foliated into a family of invariant tori $\mathbb{T}^n \times \{p\}$ for each $p \in I \subseteq \mathbb{R}^n$. We consider only integrable Hamiltonians with a *non-degenerate* frequency map, that is, $\det \partial_p^2 H^0 \neq 0$. Now, KAM deals with Hamiltonians of the form

$$H(q,p) = H^0(p) + \varepsilon H^1(q,p),$$

where $1 \gg \varepsilon > 0$ is considered small, H^0 is the integrable part and H^1 is the perturbation. We assume that H is 2π-periodic in each component of q. What KAM theory ensures is that under the correct conditions, a "large" subset $\Omega_{\gamma,\tau} \subseteq \Omega$, $\gamma, \tau > 0$ of invariant tori of $H^0(p)$ are preserved, though possibly deformed, under the perturbation H^1. The set $\Omega_{\gamma,\tau}$ is given by:

$$\Omega_{\gamma,\tau} = \bigcap_{\substack{k \in \mathbb{Z} \\ k \neq 0}} \left\{ \omega \in \Omega : |\omega \cdot k| \geq \gamma |k|^{-\tau} \right\}. \tag{4}$$

The condition for $\Omega_{\gamma,\tau}$ is called the *small divisor condition*. It can be shown for $\tau > n-1$ that for almost all $x \in \mathbb{R}^n$ there exists a $\gamma > 0$ such that $x \in \Omega_{\gamma,\tau}$, so

in particular, we can find $\gamma > 0$ so that a point $\omega \in \Omega$ satisfies $\omega \in \Omega_{\gamma,\tau}$. We finally consider the *Cantor* set

$$\hat{\Omega}_{\gamma,\tau} = \Omega_{\gamma,\tau} \cap \{\omega \in \Omega : d(\omega, \partial\Omega) \geq \gamma\},$$

that is, we remove points in $\Omega_{\gamma,\tau}$ that have distance less than γ from the boundary of Ω. It can be shown $\Omega \backslash \bigcup_{\gamma>0} \hat{\Omega}_{\gamma,\tau}$ is a set of measure zero, so the measure of $\hat{\Omega}_{\gamma,\tau}$ becomes large for small γ ,justifying the term "large". We can now give the KAM theorem as stated in [Pö82].

Theorem 1. Let the integrable Hamiltonian $H^0 : \mathbb{T}^n \times I \to \mathbb{R}$ be real analytic and non-degenerate, such that the frequency map $\partial_p H^0 : I \to \Omega$ is a diffeomorphism and let the perturbed Hamiltonian $H = H^0 + \varepsilon H^1$ be of class $C^{\alpha\lambda+\lambda+\tau}$ with $\lambda > \tau + 1 > n$ and $\alpha > 1$. Then there exists a positive γ-independent δ such that for $|\varepsilon| < \gamma^2\delta$ with γ sufficiently small, there exists a diffeomorphism

$$\mathcal{T} : \mathbb{T}^n \times \Omega \to \mathbb{T}^n \times I,$$

which on $\mathbb{T}^n \times \hat{\Omega}_{\gamma,\tau}$ transforms the equations of motion of H into

$$\dot{\theta} = \omega, \qquad \dot{\omega} = 0.$$

The map $\mathcal{T}$ is of class C^α for non-integer α and close to the inverse of the frequency map; its Jacobian determinant is uniformly bounded from above and below. In addition, if H is of class $C^{\beta\lambda+\lambda+\tau}$ with $\alpha \leq \beta \leq \infty$, then one can modify $\mathcal{T}$ outside $\mathbb{T}^n \times \hat{\Omega}_{\gamma,\tau}$ so that $\mathcal{T}$ is of class C^β for noninteger β.

So, for $\omega \in \hat{\Omega}_{\gamma,\tau}$, we parametrize an invariant torus via the map $\theta \mapsto \mathcal{T}(\theta, \omega)$. There are a few theorems in use now that are titled the *KAM theorem*, and they differ mainly whether they discuss analytic or smooth perturbations. It is easier to find sources discussing the analytic versions, since they provide stronger results about the invariant torii. Having said this, we use the C^r version because it is easier to construct smooth approximations of discontinuous functions as opposed to analytically approximating them. We bring smooth approximations into the mix, since (1) alone is discontinuous.

2.2 Approximating locally L^1 functions

The Hamiltonian (1) we wish to study is discontinuous, which by itself is not suitable for the KAM theorem. We can, however, smoothly approximate the Hamiltonian by using *mollifiers*. The KAM theorem then can be applied to the smoothed Hamiltonian, which of course means we are not directly studying (1) but instead gaining an intuition for the true behavior.

The *standard mollifier* $\varphi : \mathbb{R}^n \to \mathbb{R}$ is the following function:

$$\varphi(x) = \begin{cases} c \exp\left(\frac{1}{|x|^2-1}\right), & |x| < 1 \\ 0, & |x| \geq 1, \end{cases}$$

where $c > 0$ is a scaling factor chosen so that the integral of φ over $\mathbb{R}^n$ is 1. Also, φ is commonly called a *bump* function, since its support is compact. For $\varepsilon > 0$, let

$$\varphi_\varepsilon(x) = \frac{1}{\varepsilon^n}\varphi\left(\frac{x}{\varepsilon}\right),$$

this function has the following properties:

$$\varphi_\varepsilon \in C_c^\infty(\mathbb{R}^n), \quad \varphi \geq 0,$$
$$\int_{\mathbb{R}^n} \varphi_\varepsilon = 1, \quad \operatorname{supp}(\varphi_\varepsilon) \subset B_\varepsilon(0) = \{x \in \mathbb{R}^n : |x| < \varepsilon\},$$

that is, the function φ_ε is smooth in $\mathbb{R}^n$ with compact support, it is positive, its integral is 1, and the support of φ_ε is fully contained in the unit ball of radius $\varepsilon > 0$ centered at the origin.

Let $f \in L^1_{\text{loc}}(X)$ be a locally integrable function in $X \subseteq \mathbb{R}^n$. The *mollification* of f is defined as the convolution of f with φ_ε, that is, $\varphi_\varepsilon * f : X_\varepsilon \to \mathbb{R}$ where $X_\varepsilon = \{x \in X : d(x, \partial X) > \varepsilon\}$. Explicitly,

$$\begin{aligned} f_\varepsilon(x) = \big(\varphi_\varepsilon * f\big)(x) &= \int_X \varphi_\varepsilon(x-y) f(y) dy \\ &= \int_{B_\varepsilon(0)} \varphi_\varepsilon(y) f(x-y) dy, \quad x \in X_\varepsilon \end{aligned}$$

Some properties that the mollification f_ε has are summarized here:

Theorem 2. Let $f \in L^1_{\text{loc}}(X)$. Then the mollification f_ε has the following properties:

1. $f_\varepsilon \in C^\infty(X_\varepsilon)$,
2. $f_\varepsilon \to f$ almost everywhere as $\varepsilon \to 0$,
3. if f is continuous on X, then $f_\varepsilon \to f$ as $\varepsilon \to 0$ uniformly on compact subsebts of X,
4. if $1 \leq p < \infty$ and $f \in L^p_{\text{loc}}(X)$, then $f_\varepsilon \to f$ as $\varepsilon \to 0$ in $L^p_{\text{loc}}(X)$

Proof. The proof of this theorem can be found in Appendix C of [Eva98] ■

What we gain from Theorem 2 is not only a smooth approximation of our discontinuous Hamiltonian but an approximation that can be made arbitrarily precise almost everywhere. Of course, the points which cannot be approximated accurately are concentrated at the boundary of each disk, where the discontinuities lie. Despite this, it is reasonable to assume that for sufficiently small values of ε, the flow of the equations of motion provided by the mollified Hamiltonian approximate the flow of the disconitinuous one very well.

2.3 Investigating small magnetic field strengths

In fig. 2 we numerically solve the system and observe some interesting relations. Each plot shows 5 trajectories varying $b = 10^{-1}, \ldots, 10^{-5}$. In fig. 2a and fig. 2b the init. cond. and params. are the same $X \approx (0.38, 0.81)$ and $V \approx (0, 1)$, and $R = 1/3$, only the duration of the simulation is longer in fig. 2b. In fig. 2c, V is the same, $X \approx (0.44, 0.65)$ and $R = 1/6$.

First, we see in each figure the trajectory for $b = 0.1$ appears as a smear near the origin, this is likely because b is large enough for the deflection in each disk to be significant. We note, however, in later sections we also find circle-like quasiperiodic trajectories for significantly larger values of b. The difference here

is that these circular arcs seem to be generic, while for larger b the circle-like trajectories are more scarce and each has a smaller region of stability.

For the other values of b, we see the trajectories follow a circular arc, and for smaller b the radius of the respective circular arc is larger. In the limit $b \to 0$, the trajectories will straighten out, since the magnetic field vanishes. These two observations motivates the use of KAM, specifically, considering (1) as a perturbation of either free motion or of a uniform magnetic field in the plane.

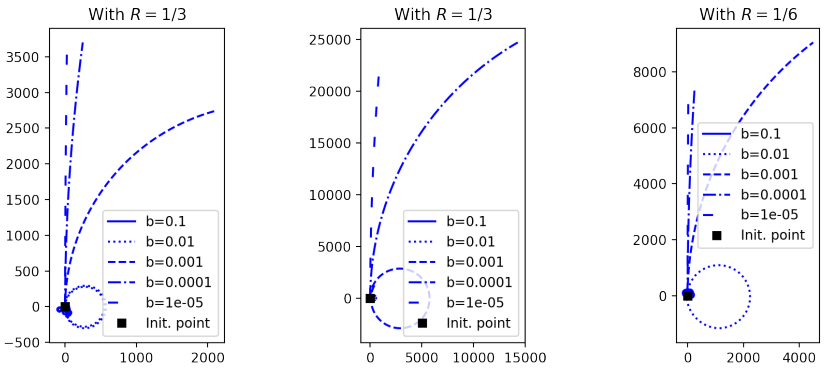

(a) (b) (c)

Figure 2: Trajectories for various choices of R and small b.

We note that the free motion perturbation idea seems to be less robust than the uniform field idea. For any small $b > 0$, we can expect that after a sufficiently long time t the accumulated deflection is substantial, for example, compare the trajectory for $b = 0.0001$ in fig. 2a and fig. 2b. Having said that, it is not visible in the figure but what appear as circular trajectories in fact do not close either, the displacement is simply very small, but this is precisely what motivated the previous comment: the circles stay circular for longer.

2.4 Perturbations of linear motion

Recall, that a particle in the plane moves along Larmor circles when in the presence of a uniform magnetic field, with strength b, orthogonal to the plane of motion. The Larmor radius R depends inversely with respect to the field strength, $Rb \propto 1$, that is, a weaker the field strength corresponds to a larger Larmor radius. So, as $b \to 0$, we expect $R \to \infty$, which means that locally the trajectory approaches linear motion in the plane. This intuition is coroborated when considering the Hamiltonian (1) and setting $b = 0$. Hence, it is natural to consider the Hamiltonian $H_0(q, p) = \|p\|^2/2$ and perturb it.

We see H_0 is real analytic, it is also in action-angle coordinates from which we can deduce it is non-degenerate $\det \partial_p^2 H_0 = 1 \neq 0$, and the frequency map $\partial_p H_0(p) = p$ is a diffeomorphism. Now, we attempt to isolate H_0 in (1) from

the perturbation term. Writing $A = (A_1, A_2, A_3)$, we see:

$$\begin{aligned} H(q,p) = \frac{1}{2}\left\|p - A(q)\right\|^2 &= \frac{1}{2}\left(p_1 + A_1(q)\right)^2 + \frac{1}{2}p_2^2 \\ &= \frac{\|p\|^2}{2} + \frac{1}{2}\left(2p_1A_1(q) + A_1^2(q)\right) \\ &\overset{(\star)}{=} H_0(p) + bH_1(q,p,b) \end{aligned}$$

where in $(\star)$ we used that we can factor out b from $A_1(q)$. As previously discussed, H_1 is discontinuous, so to apply KAM, we need to mollify H_1. Hence, consider the mollified perturbation $\hat{H}_1 = \varphi_\varepsilon * H_1$, where $\varepsilon > 0$ is a parameter independent of b. Now, by Theorem 1, for sufficiently small $b > 0$ there are tori of H_0 that are preserved under the perturbation H_1.

2.5 Perturbation of motion in a constant field

We first reason heuristically to see that this idea is valid. Comparing the trajectories for $b = 0.01$ and 0.001 in fig. 2a and 2b, we see that the radius of the trajectory is ≈ 250 and ≈ 2500, respectively. If we assume this is the value of the Larmor radius $\hat{L}$ in each case, then we see $\hat{L} \propto 1/b$ or $\hat{b} \propto b$. Now, comparing the trajectories for $b = 0.01$ in fig. 2a and 2c, we see halving the radius R of the magnetic bumps roughly quadruples the radius $\hat{L}$ from 250 to 1000, that is, $\hat{L} \propto 1/R^2$, and the strength then relates as $\hat{b} \propto R^2 b$. The task then is to determine $C \in \mathbb{R}$ such that $\hat{b} = CR^2 b$.

We can reason another way. Focusing on $[0,1]^2$, we would like the uniform field $\hat{\mathbf{B}} = \nabla \times \hat{A} = (-\hat{b}q_2, 0, 0)$ to deflect trajectories as would $\mathbf{B} = \nabla \times A$. How much a trajectory is deflected depends on the flux of the field, since the flux measures the "flow" of the field through a surface. Equating the fluxes $\Phi_{\mathbf{B}} = \Phi_{\hat{\mathbf{B}}}$, we can compute the required strength $\hat{b}$ for $\hat{B}$. The flux of $\mathbf{B}$ through a bounded region in the plane is given by:

$$\Phi_{\mathbf{B}} = \iint_S \mathbf{B} \cdot dA = \iint_S \nabla \times A \cdot dA = \iint_S (0,0,b) \cdot (0,0,1) dA = bA(S),$$

where $A(S)$ denotes the area of the surface. In our case, $\Phi_{\hat{\mathbf{B}}} = \Phi_{\mathbf{B}}$ implies $\hat{b} = \pi R^2 b$, which is about what we expected. Now, we should numerically test this hypothesis. To test the validity of the relation, we give two tests, the results of which can be found in fig. 3. The first test:

1. For $1 \le i \le 50$, sample (R_i, b_i) uniformly from $[0.25, 0.45] \times [10^{-10}, 10^{-6}]$
2. For R_i, b_i uniformly sample initial conditions X_{ij}, V_{ij} with $1 \le j \le 20$.
3. Using the method in [Coo93], fit a circle to the trajectory of each X_{ij}, V_{ij}, the radius of which is $\hat{L}_{ij}$. We take the average $\hat{L}_i = \sum_{j=1}^{20} \hat{L}_{ij}/20$.
4. Via a least squares method, we fit a general cubic:

$$\begin{aligned} a_0 + a_1R_i + a_2b_i + a_3R_i^2 \\ + a_4R_ib_i + a_5b_i^2 + a_6R_i^3 + a_7R_i^2b_i + a_8R_ib_i^2 + a_9b_i^3 = 1/\hat{L}_i. \end{aligned}$$

The second test is similar, we fix $R_i = 1/3$, and fit a line $a_0 + a_1 R_i^2 b_i = 1/\hat{L}_i$. We opt to fit a general cubic function to avoid any bias in reasoning. We should expect after fitting that only a_7 contributes significantly.

The coefficients of the fitted cubic surface in fig. 3a come out to

$$
\begin{aligned}
&a_0 \approx 6.7 \cdot 10^{-8}, && a_1 \approx -6.2 \cdot 10^{-7}, && a_2 \approx 6.7 \cdot 10^{-3},\\
&a_3 \approx 1.9 \cdot 10^{-6}, && a_4 \approx -5.3 \cdot 10^{-2}, && a_5 \approx -1.9 \cdot 10^{+2},\\
&a_6 \approx -1.8 \cdot 10^{-6}, && a_7 \approx 3.2, && a_8 \approx -6.6 \cdot 10^{+1},\\
&a_9 \approx -3.0 \cdot 10^{-4}, &&&&
\end{aligned}
$$

the values of a_0 to a_4, a_6 and a_9 are negligible as expected, likewise $a_7 \approx \pi$. We notice that a_5 and a_8 are quite large but we reason that the contribution of their respective monomial term is still small, since both contain a factor of b^2 which has an order of magnitude at most 10^{-6}. The coefficients of the fitted line in fig. 3b are $a_0 \approx 4.4 \cdot 10^{-10}$ and $a_1 \approx 3.12$, which can be explained in the same way. So, the relation $\hat{b} = \pi R^2 b$ seems valid, and this motivates perturbing a uniform magnetic field into the bump field.

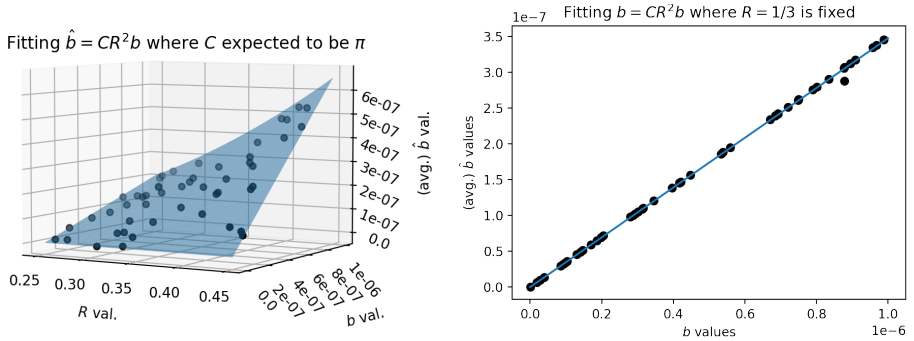

(a) Fitting a cubic surface

(b) Fitting a line

Figure 3: Plots of data and fitted polynomial models.

Overall, the results show that our assumptions are plausible, we approximately see π in the coefficient. The results are not as precise as desired but that can be due to randomly choosing the initial conditions for the trajectories. The circular trajectories correspond to invariant tori, and since not all tori are preserved under the perturbation, we expect that, chosen at random, some trajectories will not follow closely a circular path. Similarly, the chosen range for sampling R and b could be too large, though in tests we made that we omit here, we noticed that the relation holds more or less for a wider range of $[0.1, 0.45] \times [10^{-16}, 10^{-2}]$.

3 Complexity and symbolic dynamics

In this section we consider the dynamics of (1) for $b \gg 0$, that is, in the case where KAM and perturbative methods are not readily applicable. We approach the system in an exploratory way: we look for (quasi)-periodic orbits, consider their stability, and see where stability is missing.

To this end, we prove the existence of a Poincaré section, later we induce "coarse" symbolic dynamics and apply the Lempel-Ziv complexity to make sense of the dynamics. What we find is rich dynamics and a visual method of analysis well suited for similar problems.

The phase space of our system is $\mathbb{R}^2 \times \mathbb{R}^2$, however we can reduce the phase space to a Poincaré section as follows:

Proposition 1. Let S be the union of discs of radius R centered at $\mathbb{Z}^2 + 1/2$. The sets S_{in} and S_{out} defined as:

$$S_{\text{in}} = \bigcup_{x \in \partial S} \{x\} \times \{v \in \mathbb{R}^2 : v \cdot (x - 1/2) < 0\}, \tag{5}$$

$$S_{\text{out}} = \bigcup_{x \in \partial S} \{x\} \times \{v \in \mathbb{R}^2 : v \cdot (x - 1/2) > 0\}, \tag{6}$$

are Poincaré sections for the system (1).

We prove this later. This helps visualize long term behavior, since the magnitude of the velocity of a trajectory is constant. Furthermore, we can pass the system to the torus, which reduces S to one disc. So, when plotting we only need two dimensions: one to parametrize ∂S and another for the velocity.

3.1 First impressions and lots of quasiperiodicity

For the remainder of this section we fix $R = 1/3$ and $\|p\| = 1$, we only vary b. In the figures below, we collect a few periodic and quasi-periodic orbits. For each figure, on the left is a plot of the trajectory in the plane, and on the right we give the trajectory restricted to the section S_{out}. The depth of computation is 2000 entries into S_{out}, unless stated otherwise. We discovered the trajectories in fig. 4 on paper, the rest were discovered using the methods we discuss later.

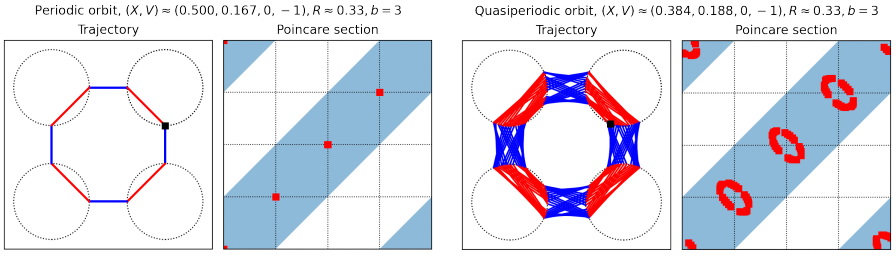

(a) (b)

Figure 4: Stable trajectories discovered analytically (more on next page).

The trajectories fig. 4a, 4c, 4e, and 4f are periodic. Figure 4a and 4c are stable, we prove this in the python notebook [??], and 4b and 4d are given by

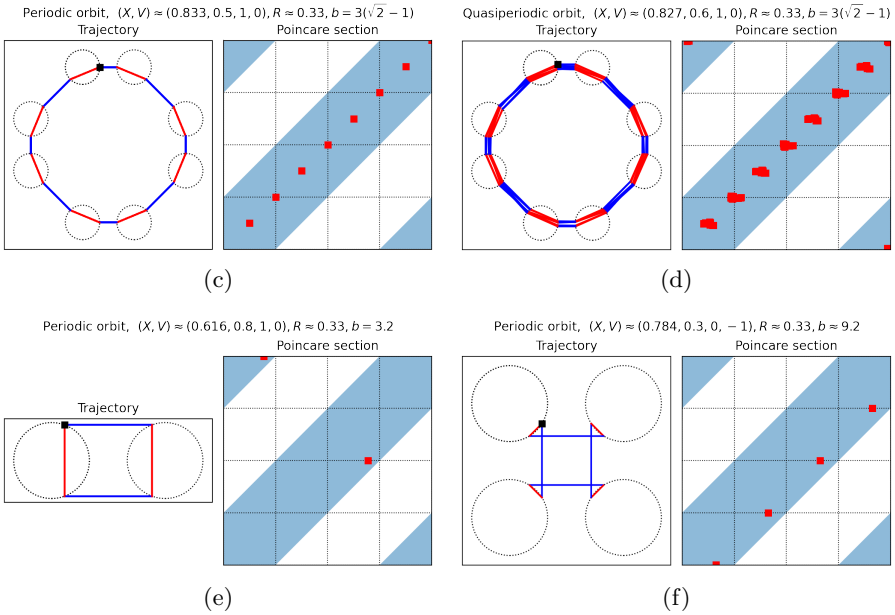

Figure 4: Unstable trajectories discovered analytically.

perturbed initial conditions of each case, respectively. Meanwhile 4e, 4f are unstable, in fact, the plots are given only to 35 iterations due to sensitivity.

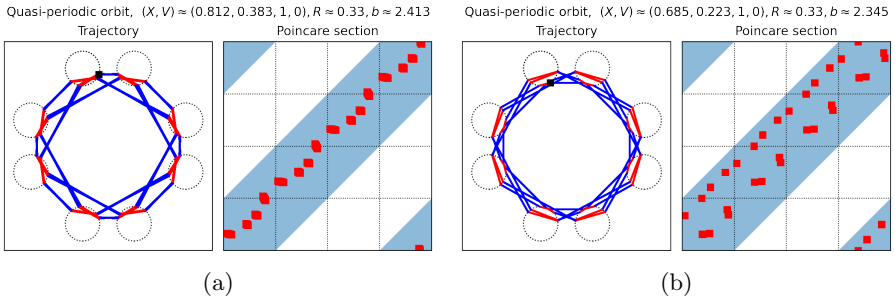

Figure 5: First signs of intricate quasi-periodicity.

Figure 5a and 5b are interesting, since they have a similar shape. The latter seems to be a "doubled" version of the former, and not a perturbation, since even after 2000 iterations the trajectory of 5b does not change, e.g., it does not smear like in the case of 4b.

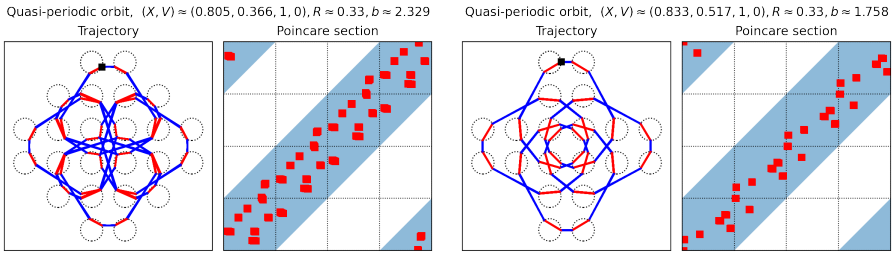

(a) (b)

Figure 6: Complex and ornamental quasi-periodic trajectories.

Figure 6a and 6b are surprisingly complex patterns, and unlike the rest of the examples, involve the most discs in the plane

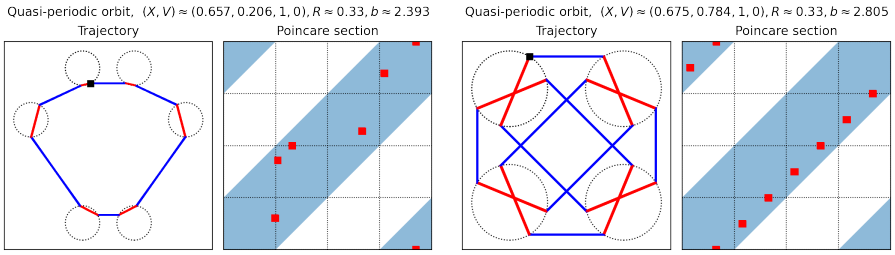

(a) (b)

Figure 7: A symmetry breaking trajectory and an honorable mention.

So far, we have seen trajectories that have square symmetries, the first to break this is 7a with a bottom-heavy hexagon. It would be interesting to see if there are other polygon, for example triangles or pentagons. Figure 7b does not illustrate anything new, we included it because it is aesthetically pleasing.

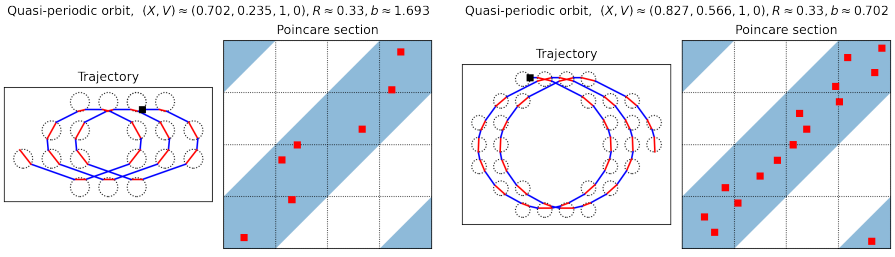

(a) (b)

Figure 8: Wandering in $\mathbb{R}^2$, yet quasi-periodic in $\mathbb{T}$.

In fig. 8a and 8b we have the first examples of trajectories that wander in the plane but are quasi-periodic in the torus. It seems that these patterns arise in between values of b that produce trajectories as in fig. 9, that is, as b decreases,

the radii of the circles in the pattern increases, and if, in a specific way, the circle does not close, you can still see repetition.

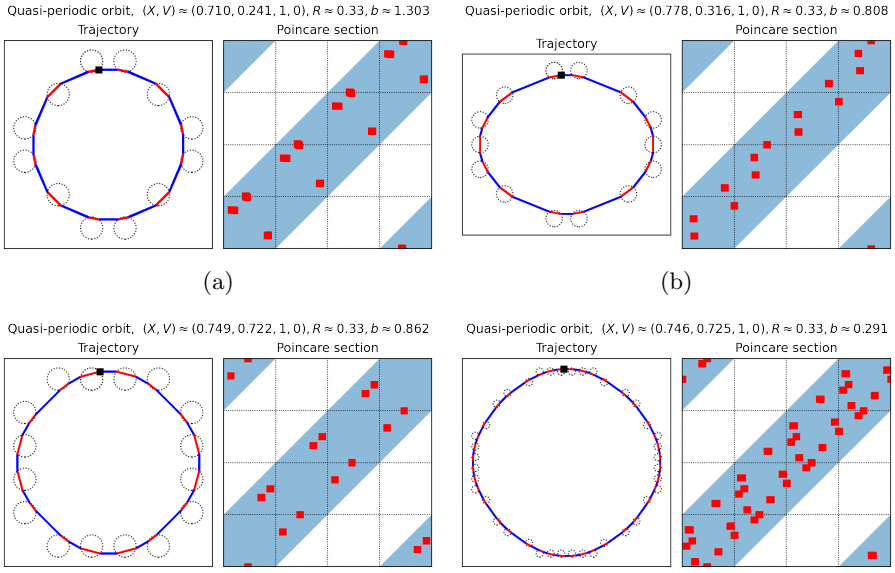

Figure 9: Large circular trajectories for small values of b.

The last 9a - 9d are examples with values of b relatively small compared to the rest. The lower the value of b, the closer the shape resembles a circle, which is in line with what we had seen using KAM. We have not found any intricate patterns for low values of b.

We see that in this simple system there is interesting dynamics with varying levels of complexity. It is safe to say that at least some of these would be hard to find by hand, and would be feasible only with some numerics and a measure of complexity for determining good candidates. We now construct the Poincaré section S_{in} and after that we outline the methods we used to obtain these quasi-periodic trajectories.

3.2 Constructing a Poincaré section

To construct the Poincaré section, we will use well known results about rotations on the torus. Parametrize the torus $\mathbb{T}$ with angles $\theta, \varphi \in [0, 1]$, a particle in free motion on $\mathbb{T}$ follows the trajectory $r(t) = x_0 + vt$ where $x_0 \in \mathbb{T}$ is the initial condition and $v \in \mathbb{R}^2$ is the velocity. If the angle of v with respect to the axis θ is rational, then $r(t)$ is periodic, otherwise $r(t)$ is dense in $\mathbb{T}$.

Lemma 1. The flow of (1) induces a well-defined map $P_{\text{oi}} : S_{\text{out}} \to S_{\text{in}}$.

Proof. Let $(x, v) \in S_{\text{out}}$, at this point the solution of (1) continues with free motion $r(t) = x + vt$. If the angle of v is rational, then there exists some time t_2 at which $r(t_2) = x$, and $(r(t_2), v) \in S_{\text{out}}$. Since at time t_2 the trajectory intersects ∂S transversally, there must exist $t_1 < t_2$ such that $(r(t_1), v) \in S_{\text{in}}$.

Since the trajectory intersects S_{in} at least once, there must exist a unique $t_0 \leq t_1$ such that $(r(t_0), v) \in S_{\text{in}}$.

If instead the angle of v is irrational, consider an open neighborhood $U \subseteq \partial S$ of x such that $U \times \{v\} \subseteq S_{\text{out}}$. This can be done by taking a sufficiently small interval in ∂S around x. Since $r(t)$ is dense in $\mathbb{T}$, there exists a time t_1 such that $r(t_1) \in U$. By the same reasoning as in the previous case, there exists a unique time t_0 such that $(r(t_0), v) \in S_{\text{in}}$.

Define $P_{oi}(x, v) = (r(t_0), v)$, which is well-defined. ■

Lemma 2. The flow of (1) induces a well-defined map $P_{\text{io}} : S_{\text{in}} \to S_{\text{out}}$.

Proof. Let $(x, v) \in S_{\text{in}}$, under the flow of (1) the trajectory $r(t)$ follows some Larmor circle C. We know $x \in C \cap \partial S$, so since (x, v) is transversal to ∂S, there must exist a point $x_1 \in C \cap \partial S$ with $x_1 \neq x$. Hence, also there must exist a time t_0 at which the trajectory intersects S_{out}. Define $P_{\text{io}}(x, v) = (r(t_0), r'(t_0))$. ■

Proof of proposition 1. The map $P_{\text{i}} = P_{oi} \circ P_{\text{io}}$ is a return map for S_{in}. Likewise, $P_{\text{o}} = P_{\text{io}} \circ P_{oi}$ is a return map for S_{out}. ■

The proof of lemma 1 does not depend on the shape of the magnetic region. However, it is not clear what needs to be changed to make lemma 2 work for arbitrary regions.

In [KS17] a similar result is proved for a configuration of finitely many bumps. In that case a different method was used that did not rely on an infinite number of bumps, in ours the reasoning was simplified due to this.

3.3 The Lempel-Ziv compression algorithm

In the previous section we discretized the continuous time system via a Poincaré map, and studied some examples of (quasi)-periodic orbits directly. To study the discrete system further, a typical approach taken is to construct a Markov partition, and to pass to a symbol space with a shift map. Providing a Markov partition in our case proved more complicated than expected. We need a better understanding of the (un)stable manifold of a point $x \in S_{\text{out}}$. Furthermore, it is not exactly clear how to "carve" up S_{out} in the first place.

To avoid this, we decided to introduce the Lempel-Ziv complexity as described in [LZ76]. The Lempel-Ziv complexity operates on finite length sequences of symbols by applying a compression algorithm, the complexity of the original sequence is then quantified by the result of the compression. Partitioning S_{out} and prescribing an alphabet is still an issue but we first discuss Lempel-Ziv.

To explain the algorithm, we use a series of examples, as in the paper [KS87]. We are not interested in the technicalities of the original paper by Lempel and Ziv, so we only cite results when needed.

Consider a sequence $s = s_1 s_2 \dots s_n$ of length $n \in \mathbb{N}$, the algorithm decides what is the smallest number of "words" in the sequence necessary for reconstruction. Suppose we have reconstructed s up to the index $k < n$ and the word counter is c, that is, we have $s_1 \dots s_k$. For the next iteration, the algorithm decides what is the largest $k < \ell \leq n$ such that the subsequence $s_{k+1} \dots s_\ell$ appears at some index in $s_1 \dots s_{\ell-1}$. Once this ℓ is found, the word counter is increased to $c+1$. If $\ell = n$, then the algorithm terminates, otherwise the process

is repeated with $s_1 \dots s_{\ell+1}$. We provide an example below. The $\cdot$ is used as a delimiter between words, the top line indicates the longest subsequence found at each iteration, and the bottom line shows where they can be found.

$$\begin{aligned}
\overline{0}1011010001101110010 &\xrightarrow{(1)} 0 \cdot \overline{1}011010001101110010 \\
&\xrightarrow{(2)} \underline{0 \cdot 1} \cdot \overline{01}1010001101110010 \\
&\xrightarrow{(3)} \underline{0 \cdot 1 \cdot 0}11 \cdot \overline{010}001101110010 \\
&\xrightarrow{(4)} 0 \cdot 1 \cdot \underline{011 \cdot 01}00 \cdot \overline{01101}110010 \\
&\xrightarrow{(5)} 0 \cdot 1 \cdot 011 \cdot 0\underline{100} \cdot 011011 \cdot \overline{100}10 \\
&\xrightarrow{(6)} \underline{0} \cdot 1 \cdot 011 \cdot 0100 \cdot 011011 \cdot 1001 \cdot \overline{0} \\
&\xrightarrow{(7)} 0 \cdot 1 \cdot 011 \cdot 0100 \cdot 011011 \cdot 1001 \cdot 0
\end{aligned}$$

At the start, we scan from the left, and notice we have never encountered a 0, so for step (1) we add 0 on its own. Next, we encounter 1 for the first time, and add it in step (2). Next, we see that we have encountered 01, so we add 011. Notice, how we ignore the delimiter between words. We indicate the rest of the steps without commentary. Once the algorithm terminates, we see that the number of words is 7, so the complexity of this sequence is 7.

The complexity is not normalized to $[0, 1]$, this is not needed since we only ever consider finite length sequences and those clearly have bounded LZ complexity. Comparing two sequences of varying length, the sequences can have the same complexity, though it is expected that the longer sequence will have a higher complexity. Now, that we have an idea how the Lempel-Ziv (LZ) complexity is computed, we can discuss how LZ captures the regularity (or lack of it) in symbolic dynamics.

Suppose for now, we have a map taking orbits of a system to elements of a symbol space, then we can distinguish three levels for LZ complexity: high, low, and intermediate. Since LZ is not normalized, and varies depending on the length of the sequences we consider, it is best to work with sequences of the same length. Furthermore, provided we fix the length, the boundary between cases is not well defined. A rule of thumb is to judge the level by comparison, for each system there will be an average complexity for a sampling of orbits, so low complexity will be well below the average and high will be well above. The average can be skewed depending on the sampling but this should be discussed on a case by case basis.

We can characterize the orbits by their complexity as follows:

- If a sequence has high complexity that means we cannot reconstruct the sequence from a small number of words. A word corresponds to some substructure in the orbit, and if there are many unique substructures, we should expect the orbit to be disorganised or chaotic.

- If the complexity is low, meaning very few words are required to reconstruct the sequence, then the corresponding orbit should be regular and

repetitive. So, we would expect a (quasi)-periodic orbit to have a low complexity.

- For intermediate complexity the scenario can be mixed. The orbit can appear mostly random with intermitent sections of structure. The orbit can also be (quasi)-periodic but with a significantly longer period for recurrence than an orbit with low complexity.

Of course, this in not formal reasoning and just an intuitive approach. An example where our reasoning breaks down is if a periodic orbit requires n symbols to describe one period and we only sampled n symbols. In this case the complexity can look high, instead of low as one would expect from a periodic orbit. In practice, we find it easy to work around these limitations as will be shown in the next section.

3.4 Partitioning the Poincaré section and compression

Now, to utilize LZ we need a map from orbits to symbol sequences. We have many options here from the partitioning of the Poincaré section to the size of the alphabet, and we do not necessarily need to use a Markov partition for LZ to give us good results. We decided to use a relaxed approach.

Consider the system in the plane, now via the pullback from the torus, S_{out} becomes the outward-pointing boundary of circles centered at lattice points. We know by lemma 1 that a point $x \in S_{\text{out}}$ is mapped to another point on ∂S. We disregard the exact point and velocity of $P_{\text{oi}}(x)$ and only record the relative position of the new circle we intersected. For example, if we have initially $x, v = (1/2, 5/6, 0, 1)$, so we are on the circle centered at $(1/2, 1/2)$, then $P_{\text{oi}}(x, v) = (1/2, 7/6, 0, 1)$ which is on the circle centered at $(1/2, 3/2)$, the symbol we record here is $(1/2, 3/2) - (1/2, 1/2) = (0, 1)$. We see immediately there are infinitely many such pairs $(n, m) \in \mathbb{Z}^2$ that we can attain. We argue that this is not a problem for computing LZ, since there can only be finitely many of these pairs in a finite sequence anyway, i.e, the complexity of a sequence is capped by its length. Another way to look at it: the pairs $(n, m) \in \mathbb{Z}^2$ are words constructed using a finite alphabet $i \in \mathbb{Z}$ with $|i| \leq 9$, so we can unpair the coordinates and work with a stream of integers.

An example to get the idea. Consider the orbit in **??**, the orbit goes down, left, up, right, and repeats, so in symbols that is

$$((0, -1), (-1, 0), (0, 1), (1, 0), \dots),$$

and this pattern repeats indefinitely. To compute LZ, we take a finite slice, for example the first 20 symbols. If computed correctly, LZ should be 5, we record the first 4 symbols as words, and the 5th word is the rest of the 16 symbols, since they just repeat the first 4. The complexity in **??** is also 5, though in **??** and **??** the complexity is 9. We notice also that if we took the first 100 symbols of these orbits, the complexity would still be 5 and 9, respectively, provided they are stable (quasi)-periodic orbits.

3.5 Examples and thoughts

We now look at some examples. We find LZ performs well when we compute it for a range of initial conditions and parameters.

Consider again the examples from **??** and **??**, the second one was obtained by slightly perturbing the initial position and this hints that the periodic trajectory is stable. We ask now how much can we perturb the initial conditions before we leave the region of stability for this periodic orbit. We take $R = 1/3, b = 3$ and compute LZ for the family of intial conditions:

$$x = \left(\frac{1}{2} + \sqrt{R^2 - y^2}, \delta\right), \quad v = (1, 0), \qquad \text{for } y \in [-0.32, 0.32] + \frac{1}{2},$$

that is, we keep the velocity the same, and we sweep the right half-circle centered at $(1/2, 1/2)$. We report the results in fig. 10a. We see that the region spans values of y roughly in $[0.346, 0.653]$. We also notice there are some dips outside the region of stability. Out of curiosity we plot the orbit of the far left dip in fig. 1, interestingly, the orbit at first is scattered and then gets trapped between four bumps. Later, we computed more iterations of the orbit and noticed it eventually leaves the four bumps, so it seems the orbit came close to the stable region but did not enter it.

In fig. 10b we instead fix the initial conditions $x, v = (5/6, 1/2, 1, 0)$ and vary $b \in (0.001, 10)$. We see that near $b = 4$, LZ is consistently high, while for $b < 4$ there are some dips: the dips that contain $b = 3$ and $b = 3(\sqrt{2}-1) \approx 1.25$ should correspond to the regions of stability for the orbit in **??**, and **??**, respectively. There are other dips in the plot, however we ignore them, they could either be comparatively small stable regions or one of the few "false positives" that we discussed before.

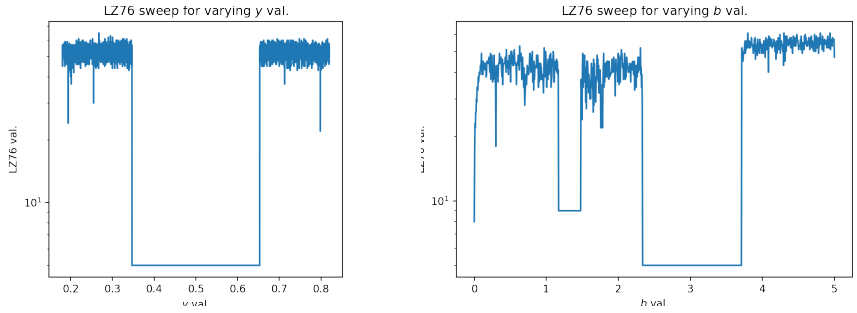

(a) (b)

Figure 10

If instead we sample a grid of points on the Poincaré section S_{out}, we can compute LZ as in fig. 11a. We only compute LZ for a strip of the Poincaré section, specifically, for $\theta \in [-\pi/4, \pi/4]$, since the rest of the picture can be reconstructed via translation. This corresponds to the 4-fold rotational symmetry of a square lattice, that is, if we rotate $\mathbb{R}^2$ at the origin by an angle of $n * \pi/2$ for $n = 0, \ldots, 3$, the lattice of circles stays the same, and the resulting dynamics are the same as well.

In fig. 11a we compute LZ for $R = 1/3$ and $b = 3$. We see a large stable "eye" at $(\theta, \varphi) = (0, 0)$. This is not unexpected, since we've seen evidence for a large stable region in fig. 10a. Besides the eye, we see some lines that have intermediate complexity, and on those either lie unstable periodic orbits or special occurances like fig. 1. We include some close ups of the eye: the top left

corner of the eye where we notice some obvious fractal behavior, and another spot along the boundary of the eye. We must note again that the emerging features in the images are sensitive to varying the depth of simulation. When attempting to plot the close ups, for example, the second one, we noticed that more yellow strips would appear and their width would increase the longer we simulated. The deeper we simulate, the more the boundary moves, which is not unreasonable since we capture more information.

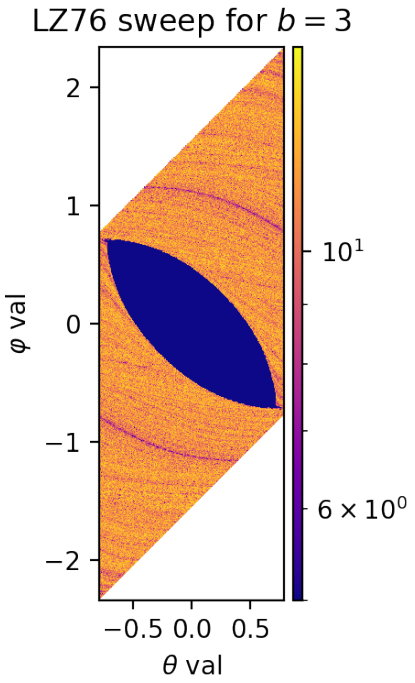

(a)

(b) placeholder

Figure 11

In fig. 12a we plot the same data except $b \approx 3(\sqrt{2}-1)$, so we plot the Poincaré section corresponding to **??**. We notice there are several very stable regions, however by comparing with **??** they should correspond to the same family of (quasi)-periodic orbits. The shape of the very stable regions is quite different, they are twisted with fractal "digits". Besides the large regions there are intermediate complexity regions scattered about, due to their globular shapes we suspect they are also relatively stable.

In fig. 13a, we pick a value of $b = 2.32$ and find a range of stable regions. Generally, the shapes are elongated, exaggerated compared to the other figures and it is not clear why this is the case. It can be noticed that there are 3 different colors for the stable regions, indicating there could be 3 different stable orbits here.

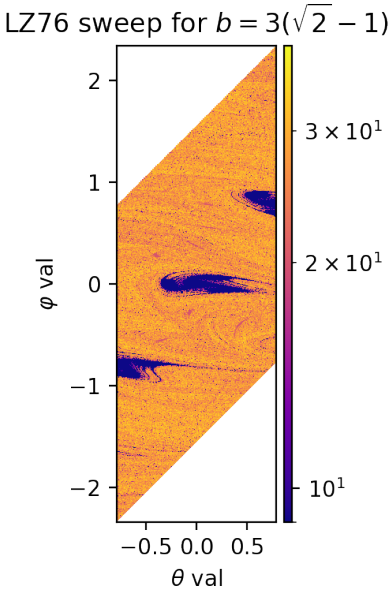

(a)

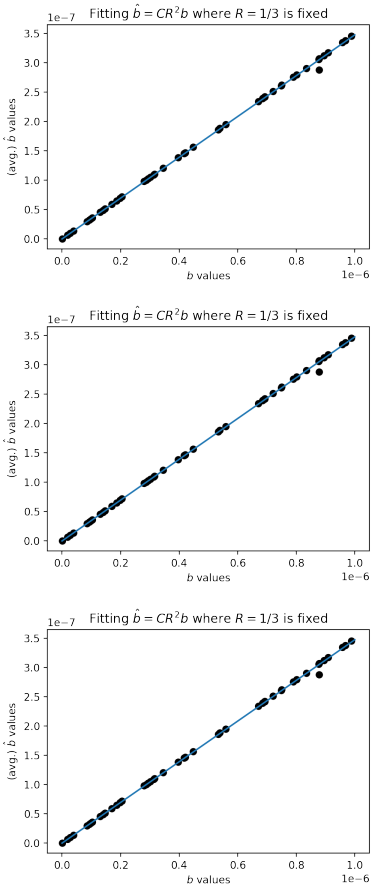

(b) placeholder

Figure 12

4 Levy Flights

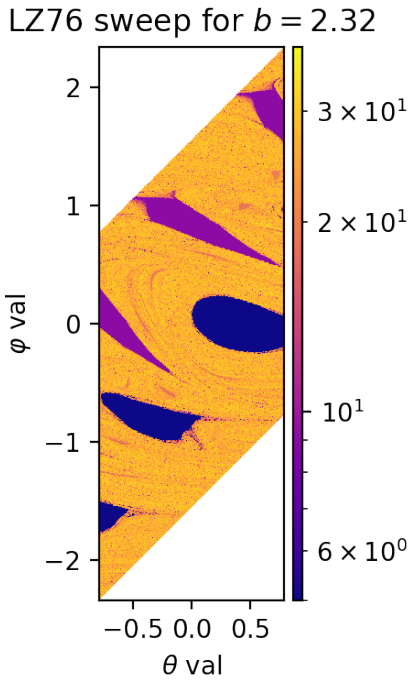

(a)

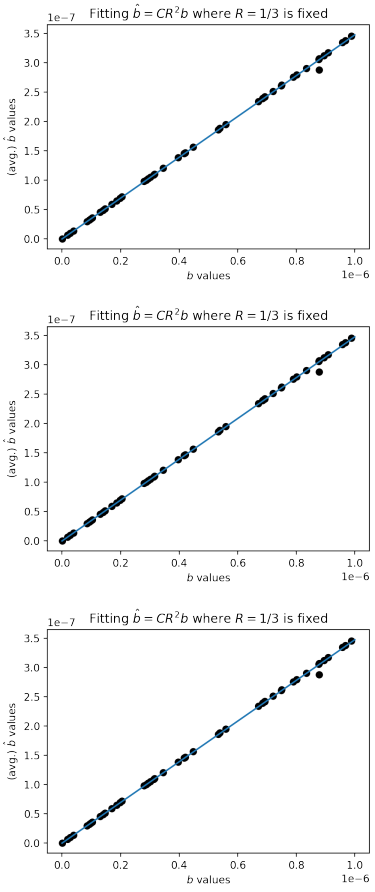

(b) placeholder

Figure 13

5 Conclusion

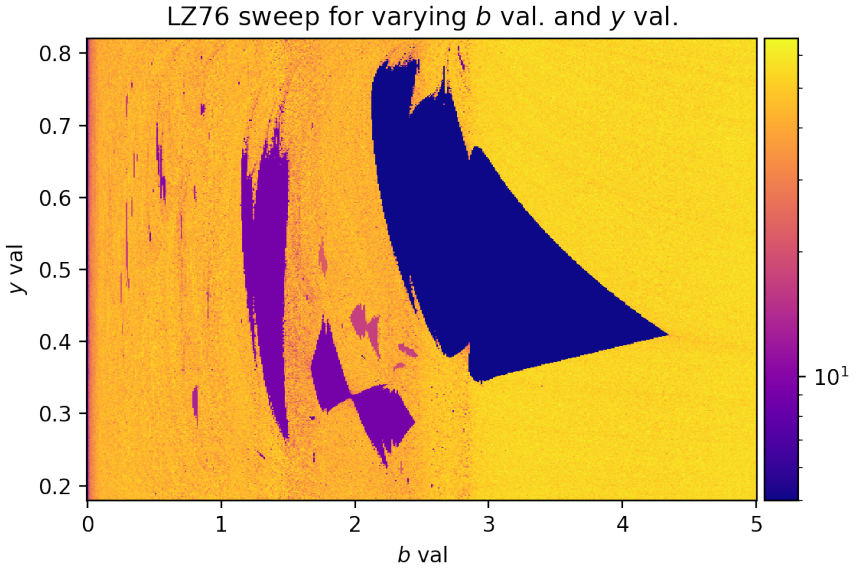

(a)

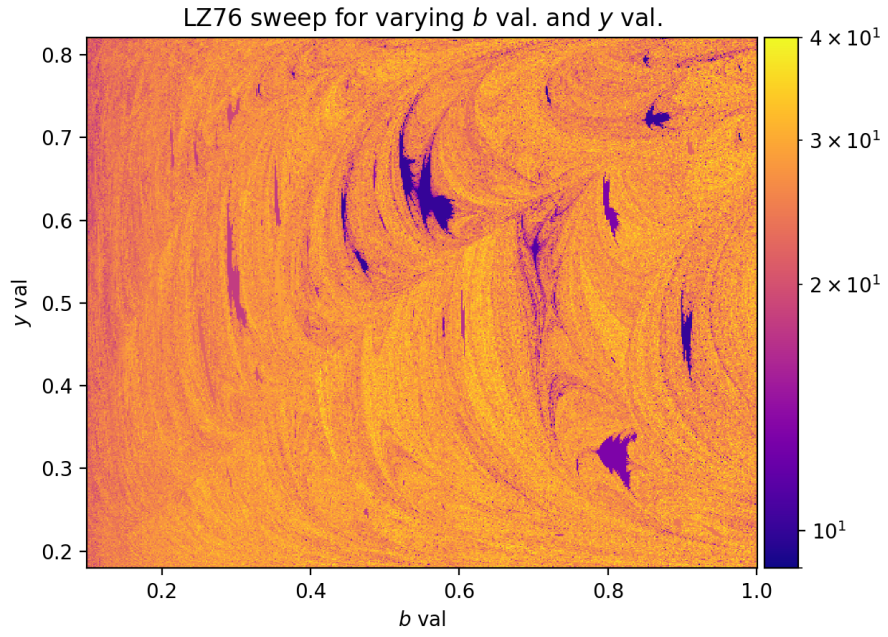

(b) placeholder

Figure 14

References

[Coo93] I. D. Coope. Circle fitting by linear and nonlinear least squares. *Journal of Optimization Theory and Applications*, 76:381–388, Feb 1993.

https://doi.org/10.1007/BF00939613.

[Eva98] Lawrence C. Evans. *Partial Differential Equations*. American Mathematics Society, 1998. Providence, RI.

[Gas21] Sean Gasiorek. On the dynamics of inverse magnetic billiards. *Nonlinearity*, 34(3):1503–1524, mar 2021. https://doi.org/10.1088%2F1361-6544%2Fabe2f1.

[Kna18] Andreas Knauf. *Mathematical Physics: Classical Mechanics*. Springer Berlin, Heidelberg, mar 2018. https://doi.org/10.1007/978-3-662-55774-7.

[KS87] Kaspar and Schuster. Easily calculable measure for the complexity of spatiotemporal patterns. *Physical review. A, General physics*, 36 2:842–848, 1987.

[KS17] Andreas Knauf and Marcello Seri. Symbolic dynamics of magnetic bumps. *Regular and Chaotic Dynamics*, 22(4):448–454, jul 2017. https://doi.org/10.1134%2Fs1560354717040074.

[LZ76] A. Lempel and J. Ziv. On the complexity of finite sequences. *IEEE Transactions on Information Theory*, 22(1):75–81, January 1976.

[Pö82] Jürgen Pöschel. Integrability of hamiltonian systems on cantor sets. *Communications on Pure and Applied Mathematics*, 35(5):653–696, 1982. https://onlinelibrary.wiley.com/doi/abs/10.1002/cpa.3160350504.

[Ser22] Marcello Seri. *Hamiltonian Mechanics*. AMS Open Math Notes, mar 2022. https://www.ams.org/open-math-notes/omn-view-listing?listingId=110861.